Defect enhanced CoMnNiO$_x$ catalysts derived from spent ternary lithium-ion batteries for low-temperature propane oxidation

Ganggang Li [a,b], Kai He [b], Fenglian Zhang [a], Guoxia Jiang [a], Zeyu Zhao [a], Zhongshen Zhang [a,*], Jie Cheng [a], Zhengping Hao [a,b,**]

[a] *National Engineering Laboratory for VOCs Pollution Control Material & Technology, Research Center for Environmental Material and Pollution Control Technology, University of Chinese Academy of Sciences, Beijing 101408, PR China*
[b] *Research Center for Eco-Environmental Sciences, Chinese Academy of Sciences, Beijing 100085, PR China*

ARTICLE INFO

ABSTRACT

Herein, a feasible strategy was reported to reuse the waste ternary lithium-ion batteries (TLIBs) as precursors to develop efficient CoMnNiO$_x$ catalysts for propane oxidation. Interestingly, the T$_{90}$ value of the defect enhanced-CoMnNiO$_x$ catalyst for propane oxidation was only 200 °C. The de-aluminum and de-lithium process generated by the alkaline etching promoted the increase of the oxygen vacancy defects, which was confirmed by ICP-OES, XPS, EPR and DFT calculations. At the atomic level, the oxygen vacancies near the aluminum and lithium vacancies (NiO-Al$_v$-O$_v$ and NiO-Li$_v$-O$_v$) were more likely to promote the activation of oxygen molecules. Furthermore, it was observed that the reducibility, acidity and lattice oxygen mobility of the defective CoMnNiO$_x$ catalyst were boosted by the presence of abundant oxygen vacancy defects, and thus enhancing the catalytic activity. Remarkably, the TLIBs recycling and defect enhancement engineering are conducive for the development of the green and efficient catalysts for VOCs oxidation.

1. Introduction

With the rapid development of energy storage devices such as electric vehicles, the lithium-ion batteries (LIBs) have a huge market demand, but also bring serious disposal dilemma of waste LIBs [1,2]. This is especially observed in the case of the ternary lithium-ion batteries (TLIBs), which are rich in the valuable metal elements, such as cobalt, manganese and nickel [3]. Thus, a feasible method to directly reuse Co, Mn and Ni without complex separation and purification process is vitally needed. The volatile organic compounds (VOCs) have received an extensive research attention owing to their widespread emission sources, environmental hazards and impacts on the human health [4]. Considering that the transition metal oxides (TMOs) possess high reducibility and excellent oxygen mobility, they have emerged as effective candidates for VOCs oxidation [5–8].

Propane is one of the main VOCs pollutants, and its emission sources are widely from petroleum refining, natural gas processing as well as coal chemical production process [9]. Because of propane's insert chemical nature and robust C—H bonds, it remains challenging to achieve propane oxidation at low temperature [10]. In a variety of catalysts, TMOs such as Co$_3$O$_4$ [11], MnO$_2$ [12], and NiO [13], exhibited good catalytic activity in propane oxidation. In particular, the synergistic effect of metal elements in dual- or multi-composite oxides on catalytic activity has been widely studied. Hu et al. synthesized NiCeO$_x$ nanosheets for the application to propane oxidation, and found that T$_{90}$ value of 4% Ce/(Ni + Ce) catalyst with the best activity was 315 °C [14]. Besides, Bae et al. deeply investigated the promoting effect of Mn-doping Co$_3$O$_4$ for propane oxidation by crystal facet regulation [15]. Nevertheless, the low-temperature activity of TMOs catalysts for propane oxidation needs to be further improved.

Defect engineering is considered an effective strategy to enhance catalytic activity due to its ability to regulate the electronic states of catalyst surface [16]. Particularly, the oxygen vacancy defects, as strong electronic donors, possess a significant potential for catalytic oxidation reaction [17,18]. In order to effectively constructing defect in TMOs, the usual methods such as chemical reduction, acid etching, physical
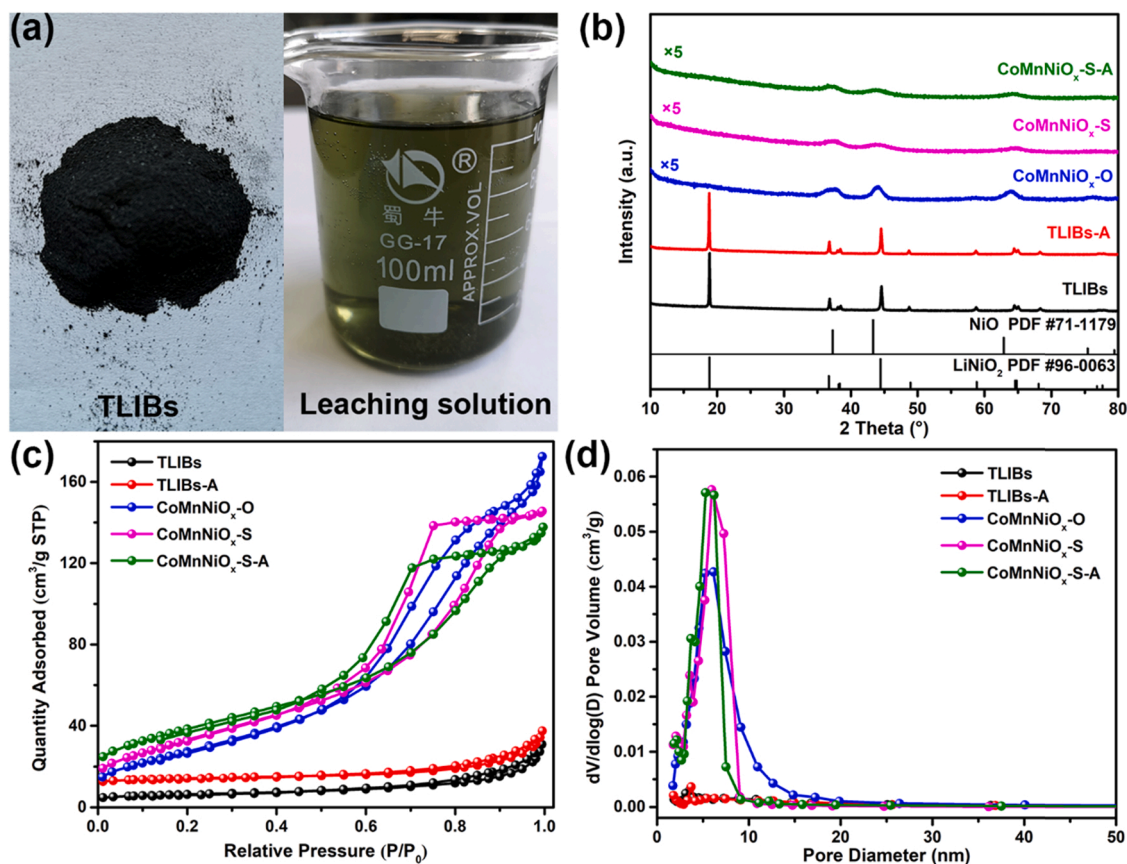

Fig. 1. (a) Physical images (b) XRD patterns, (c) N_2 adsorption-desorption isotherms and (d) pore size distributions of obtained samples from waste TLIBs.

exfoliation and etching can be adopted [19]. Among them, acid etching is used to selectively dissolve some elements, to gain the role of specific surface area augmentation and defect enhancement. Typically, $LaMnO_3$ perovskite was treated with diluted HNO_3 to selectively remove La element, gaining a MnO_2-like catalyst with high activity for CO oxidation [20]. To our best knowledge, alkaline etching for defect engineering in TMOs is rarely adopted in heterogeneous catalysis until now.

In this study, combined Co, Mn and Ni from the waste TLIBs were directly used as the precursor to develop the VOC oxidation catalysts. The type of precipitant was optimized, and a series of $CoMnNiO_x$ catalysts was subsequently synthesized for propane oxidation. In order to enhance the catalytic activity, the inert ions (Al^{3+} and Li^+) of TLIBs are utilized as the atomic defect templates for the oxygen defect engineering by employing the alkaline etching method. Moreover, based on the detailed characterizations and density functional theory (DFT) calculations, the formation and role of the oxygen vacancy defects in propane oxidation were studied in detail.

2. Experimental section

2.1. Catalysts preparation

The ternary cathode materials (NMC 622, Li $Ni_{0.6}Co_{0.2}Mn_{0.2}O_2$) were obtained from the waste LIBs of the commercial electric vehicles. The flow chart for preparing the $CoMnNiO_x$ catalysts from the waste TLIBs is shown in Scheme S1. The discharging, manual peeling and mechanical separation in the pretreatment section were carried out as reported by He et al. [21]. After ball milling and calcination to remove the graphite (500 °C for 4 h), the mixed material of aluminum powder and Li $Ni_{0.6}Co_{0.2}Mn_{0.2}O_2$ anode materials was obtained, termed as the TLIBs.

For the leaching process, 6 g TLIB powder was added into 300 mL solution containing 1 M HNO_3 and 5% H_2O_2 (solid/liquid radio of 20 g/

L). After stirring for 4 h at 30 °C, the leaching solution was collected by vacuum filtration. Subsequently, the pH value of the leaching solution was adjusted to 4 by adding 1 M NaOH solution. For the $CoMnNiO_x$-O catalyst, 150 mL of oxalate acid solution ($H_2C_2O_4$, 1 M) was added dropwise into 150 mL leaching solution, followed by stirring for 1 h. Subsequently, a green sediment was obtained by filtration. For the $CoMnNiO_x$-S catalyst, 0.5 M sodium carbonate solution (Na_2CO_3) was added dropwise into 150 mL leaching solution to adjust the pH to 10, followed by stirring for 1 h. A brown sediment was obtained by filtration. In order to avoid the interference of sodium ions, the product was washed with 500 mL of deionized water after Na_2CO_3 precipitation and NaOH etching, respectively. The washing step is repeated at least three times to ensure that the filtrate is neutral. Finally, all sediments were dried at 60 °C overnight and were calcined at 400 °C for 4 h.

TLIBs-A and $CoMnNiO_x$-S-A were obtained from TLIBs and CoMnNiO_x-S after the alkaline etching. Typically, 2 g TLIB sample (or 1 g $CoMnNiO_x$-S sample) was added into 100 mL NaOH solution (1 M), followed by stirring at 80 °C for 4 h. After filtration and drying, the catalysts were obtained by calcination at 400 °C for 4 h.

The simulated $CoMnNiO_x$ catalysts with similar chemical composition were synthesized by using chemical reagent. In the synthesis precursors of these catalysts, the molar ratio of Li:Co:Mn:Ni:Al is 10:2:2:6:8, which is similar to the ratio of dissolved TLIBs. For $CoMnNiO_x$-S catalyst, 1 M Na_2CO_3 solution was added drop by drop to the mixed metal salt solution ($LiNO_3$, $Co(NO_3)_2$, $Mn(NO_3)_2$, $Ni(NO_3)_2$, $Al(NO_3)_3$), in which the total metal concentration is 0.5 M), until the pH is 10. For $CoMnNiO_x$-O catalyst, 200 mL 1 M $H_2C_2O_4$ solution was added drop by drop to the mixed nitrate solution (same as the simulated $CoMnNiO_x$-S). Similarly, the $CoMnNiO_x$-S-A and $CoMnNiO_x$-O-A catalysts were obtained by NaOH solution etching. Besides the above, all other steps are similar to those $CoMnNiO_x$ catalysts derived from TLIBs.

Table 1
ICP-OES results of obtained samples from waste TLIBs.

Sample	Co	Mn	Ni	Li	Al	Co/Ni[a]	Mn/Ni
TLIBs[b]	11.70	13.40	36.01	7.66	2.31	0.32	0.40
TLIBs-A	11.92	13.45	36.66	7.25	1.76	0.32	0.39
CoMnNiO$_x$-O	15.94	13.28	41.71	0.19	0.09	0.38	0.34
CoMnNiO$_x$-S	12.77	14.85	39.45	0.01	2.02	0.32	0.40
CoMnNiO$_x$-S-A	13.23	15.34	40.96	0.01	1.66	0.32	0.40
Leaching solution-1[c]	1977.7	2245.8	6099.3	1274.5	303.6	0.32	0.39
Leaching solution-2[d]	0.4	0.2	0.8	131.8	207.2	–	–

[a] Molar ratio of each element.
[b] Mass percentage of each element in the prepared catalysts.
[c] Concentration of each element in leaching solution (mg/L).
[d] Leaching solution-1 and -2 represents the filtrate of TLIBs treated with acidic solution (1 M HNO_3 +5%H_2O_2) and alkaline solutions (1 M NaOH), respectively.

2.2. Catalyst characterizations

All of prepared catalysts were characterized by X-ray diffraction (XRD), Nitrogen adsorption-desorption isotherms, inductively coupled plasma atomic emission spectroscopy (ICP-OES), scanning electron microscopy-energy dispersive X-ray spectroscopy (SEM-EDS), hydrogen temperature-programmed reduction (H_2-TPR), oxygen/ammonia temperature-programmed desorption (H_2-TPR and NH_3-TPD), X-ray photoelectron spectra (XPS), electron paramagnetic resonance (EPR), ex situ/in situ Raman and in situ DRIFTS. The details of characterization program can be seen in Supporting Information.

2.3. Catalytic activity and kinetic measurements

The catalytic activity of propane oxidation was measured in a fixed-bed quartz tube reactor (4 mm i.d.) with 0.1 g of catalyst (40–60 mesh). The reactant gas, composed of 0.2% propane, 2.5% oxygen and nitrogen as balance gas, was introduced to the catalyst bed at a weight hourly space velocity (WHSV) of 18,000 mL g^{-1} h^{-1}. The reactants and products were analyzed using an Agilent 7890B gas chromatograph equipped with a hydrogen flame ionization detector (FID) for organic compounds detection and a thermal conductivity detector (TCD) for CO_2 and CO detection. The concentration of the added water vapor was regulated by reactant gas bubbling through liquid water at the desired temperature. The conversion of propane (X_{C3H8}) and the yield of CO_2 (Y_{CO2}) were calculated as follows:

$$X_{C3H8}(\%) = \left(1 - [C_3H_{8out}]/[C_3H_8]_{in}\right) \times 100 \qquad (1)$$

$$Y_{CO2}(\%) = [CO_2]_{out}/\left(3 \times [C_3H_8]_{in}\right) \times 100 \qquad (2)$$

Table 2
Textural properties and catalytic activity of synthesized catalysts.

Sample	S_{BET}[a] (m^2/g)	V_t[b] (cm^3/g)	D_p[c] (nm)	T_{50} (°C)	T_{90} (°C)	E_a (kJ/mol)[d]	E_a (kJ/mol)[e]
TLIBs	12.9	0.04	11.1	451	>600	–	–
TLIBs-A	13.3	0.04	11.6	353	491	–	–
CoMnNiO$_x$-O	127.9	0.28	6.7	186	216	69.1	74.3
CoMnNiO$_x$-S	137.0	0.24	5.5	181	214	54.2	63.5
CoMnNiO$_x$-S-A	138.7	0.22	5.2	175	200	44.1	54.7

[a] S_{BET}: specific surface area obtained by the Brunauer-Emmett-Teller method.
[b] V_t: the total of pore volume calculated by BJH desorption method.
[c] D_p: the average pore diameter obtained by BJH desorption average pore diameter.
[d] E_a: the apparent activation energy of propane oxidation calculated by Arrhenius equation at dry condition.
[e] The Ea was tested with 5 vol% H_2O.

where $[C_3H_8]_{in}$ and $[C_3H_8]_{out}$ are the inlet and outlet concentrations of propane, respectively. $[CO_2]_{out}$ is the outlet concentration of CO_2 after reaction. The detailed conditions and kinetic tests are described in Supporting Information.

2.4. Theoretical calculations

DFT calculations were applied through the Vienna ab initio simulation package (VASP). The Generalized Gradient Approximation (GGA) with the Perdew–Burke–Ernzerhof (PBE) functional was used for all the calculations. The lattice parameter of NiO bulk (4 Ni and 4 O atoms) was first optimized with the Monkhorst-Pack k-point of $6 \times 6 \times 6$. The NiO (100) surface (36 Ni and 36 O atoms) were constructed with the vacuum layer of 15 Å. A Monkhorst-Pack k-point $3 \times 3 \times 1$ was used for all surface calculations with the cut-off energy of 400 eV. The structural optimization was conducted using the conjugate-gradient (CG) algorithm, and the force convergence was set to be 0.05 eV Å^{-1}. The formation energy of oxygen vacancy was calculated following: $E_{Ov-form} = E_{slab+Ov} + 0.5E_{O2} – E_{slab}$, the adsorption energy of O_2 was calculated following: $E_{O2-ad} = E_{slab+O2} – E_{slab} – E_{O2}$.

3. Results and discussion

3.1. Composition and structure properties

The physical images of the TLIB powders and leaching solution after acid dissolution are shown in Fig. 1a. In general, the waste TLIBs contain metal shell, anode electrode, cathode electrode and organic diaphragm. After powdering and calcination process, the obtained materials are composed of TLIBs and Al foil. Therefore, the dissolved solution usually contains the Li, Co, Mn, Ni and Al elements.

The results of the elemental composition analysis by ICP-OES are tabulated in Table 1. The composition ratios of Co, Mn and Ni in all samples except CoMnNiO$_x$-O are observed to remain almost constant. It indicates that the dissolution and precipitation rates of Co, Mn and Ni elements are almost similar due to their similar chemical properties. Specially, it can be observed that the Co/Ni ratio is increased while the Mn/Ni ratio is decreased in the CoMnNiO$_x$-O catalysts, which is consistent with literature reporting that oxalic acid can preferentially promote the precipitation of the Co ions [6]. Notably, the content of Li in CoMnNiO$_x$-O is higher than that of CoMnNiO$_x$-S, indicating that Na_2CO_3 exhibits a superior ability to separate Li and other transition metal elements. On the other hand, the Al content in CoMnNiO$_x$-O and CoMnNiO$_x$-S is noted to be completely opposite to the Li content, which is attributed to the fact that the CO_3^{2-} is more likely to produce the aluminum carbonate precipitation. As is well known, Al and Li generally act as the inert impurities in the oxidizing catalysts. However, these are inevitable in the composite oxides derived from the waste TLIBs. Innovatively, the alkaline solution was used to selectively etch and remove the residual Li and Al. Importantly, the inert ions (Al^{3+} and Li^+) of TLIBs can be utilized as the atomic defect templates to produce the defect sites
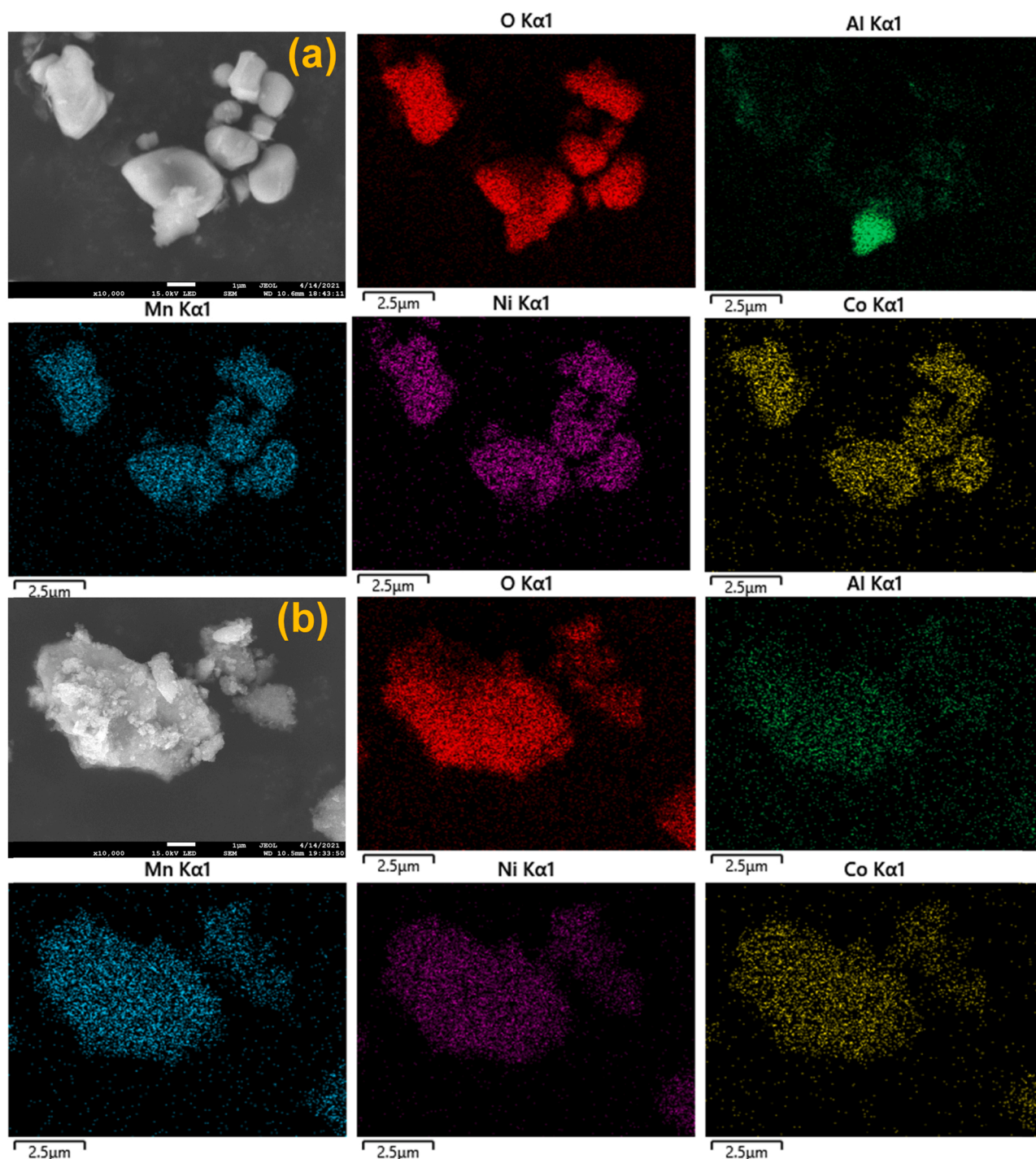
Fig. 2. EDS-mapping images of (a) TLIBs and (b) CoMnNiO$_x$-S-A catalysts.

at the same time. Based on the ICP-OES analysis of the filtrate after NaOH treatment (Leaching solution-2), it can be found that only Li and Al in CoMnNiO$_x$-S are selectively etched out.

The XRD patterns of the obtained catalysts in Fig. 1b reveal that the TLIBs and TLIBs-A catalysts maintain the main peaks at $2\theta = 18.8°$, $36.6°$ and $44.4°$, which can be assigned to the LiNiO$_2$ crystal structure (JCPDS 09-0063). The diffraction peaks of the CoMnNiO$_x$ catalysts prepared by the dissolution and re-precipitation method are widened, indicating a low degree of crystallinity or small grain size. Generally, the surface of the amorphous or small grain sized materials contains more defect sites [22]. The similar peaks at $2\theta = 37.2°$, $43.3°$ and $62.9°$ of CoMnNiO$_x$-O, CoMnNiO$_x$-S and CoMnNiO$_x$-S-A can be attributed to NiO

(JCPDS 71-1179) due to the TLIBs are rich in Ni. Furthermore, the nitrogen adsorption and desorption isotherms as well as the pore size distribution curves (Fig. 1c, d) demonstrate that the alkaline etching has no effect on the pore structure, and the specific surface area (SSA) has barely changed (Table 2).

The elemental distribution states in the catalysts are analyzed by the FE-SEM equipped with energy dispersive X-ray spectroscopy (EDS). As shown in Figs. 2 and S1, Co, Mn and Ni are uniformly distributed in the catalysts. It is worth noting that there are a few Al foil particles on the surface of the TLIBs catalyst. On the contrary, the CoMnNiO$_x$-S-A catalyst exhibits a low content and a high dispersibility of aluminum.
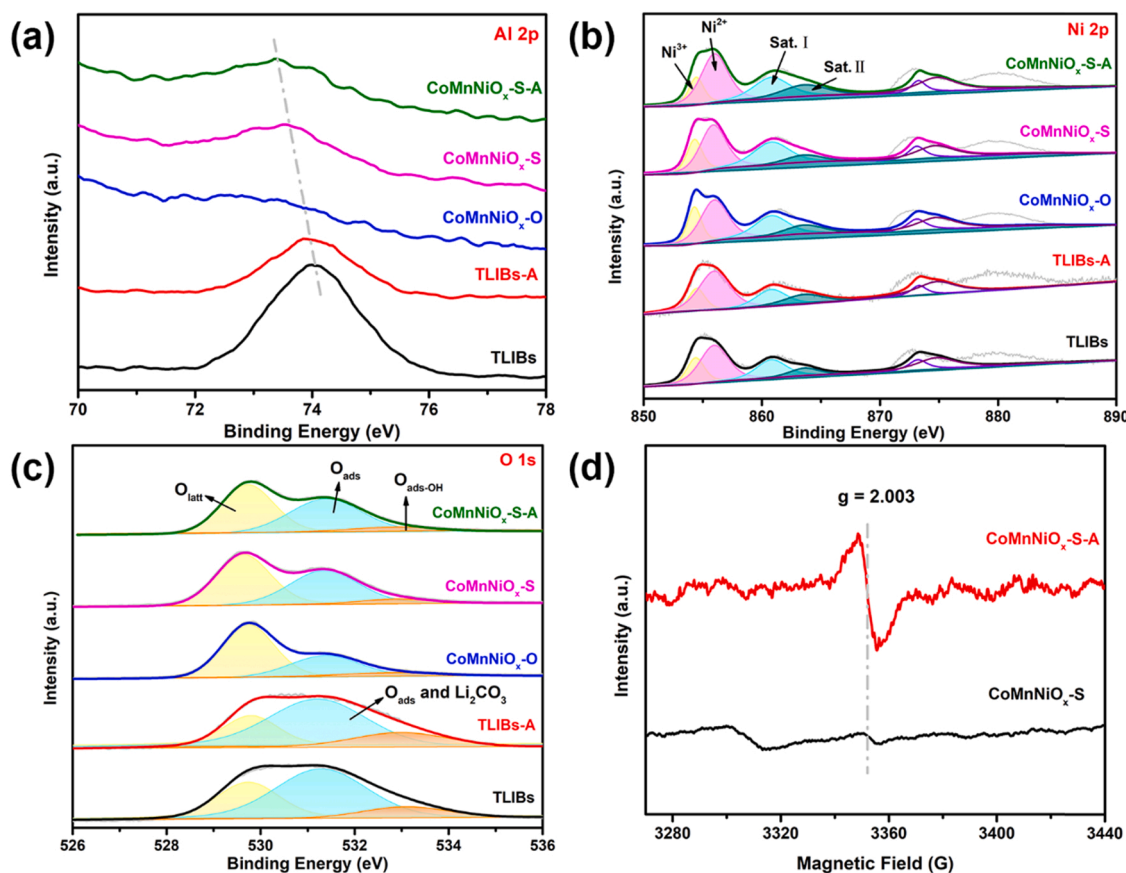
Fig. 3. XPS spectra in the (a) Al 2p, (b) Ni 2p, (c) O 1s and (d) EPR regions of prepared catalysts.

3.2. Defect enhancement engineering by de-aluminum and de-lithium process

According to the above, ICP-OES analysis reveals that the alkaline etching has successfully caused de-aluminum and de-lithium process. In order to further investigate the change of surface chemical state of the catalysts, the XPS measurements are carried out. As pictured in Fig. 3a, the reduction of aluminum content leads to the weakening of the intensity of Al 2p, and there is a significant red-shift of the binding energy in the CoMnNiO$_x$-S-A catalyst. It indicates that the coordination state of Al has changed with the de-aluminum process [23]. As reported in literature, the oxygen vacancy defects in the TMOs catalysts can be verified by the valence state of the metal element and O 1 s spectrum. As the element with the largest proportion in all catalysts, Ni 2p spectra can be classified as Ni^{3+} and Ni^{2+} with two satellite peaks, located at 854.2, 855.8, 860.8 and 863.6 eV, respectively (Fig. 3b) [24]. The creation of the oxygen vacancies in NiO can induce an increase in the proportion of Ni^{3+} that is in the higher valence state, which is contrary to Mn and Co [25,26]. The O 1 s spectra in the catalysts are divided into hydroxyl oxygen in the chemisorbed water (O$_{ads-OH}$), adsorbed oxygen in the oxygen vacancy (O$_{ads}$) or trace amount of Li$_2$CO$_3$ impurity [27], and surface lattice oxygen (O$_{latt}$), located at 533.1 eV, 531.4 eV, and 529.7 eV, respectively (Fig. 3c) [28]. To sum up, the ratio of Ni^{3+}/Ni^{2+} and O$_{ads}$/O$_{latt}$ ratios can be used as a descriptor of the oxygen vacancy defects on the prepared catalysts. Based on the semi-quantitative comparison of the obtained results (Table S1), the order of the oxygen vacancy defects can be mention as: TLIBs-A > TLIBs, and CoMnNiO$_x$-S-A > CoMnNiO$_x$-S > CoMnNiO$_x$-O. It is worth mentioning that Ni in TLIBs catalysts of type NCM 622 mainly exists with Ni^{3+} [29], and thus the Ni^{3+}/Ni^{2+} ratio is higher than that of CoMnNiO$_x$ catalysts, even though they have a lower oxygen vacancy content compared with CoMnNiO$_x$

catalysts. These results indicate that the de-aluminum and de-lithium process can significantly increases the oxygen vacancy defects in the prepared catalysts through alkaline etching.

In addition, the metal valence states of the other typical active elements (Mn and Co) are analyzed by using the Mn 2p, Mn 3 s and Co 2p spectra (Fig. S2). As reported in literature, the Mn^{3+} and Mn^{4+} peaks in the Mn 2p$_{3/2}$ spectra are situated in 641.4 and 643.2 eV, respectively [30]. The average oxidation state (AOS) of Mn can be further calculated from the binding energy difference (ΔE) of Mn 3 s, and the equation is: AOS= 8.956–1.126 * ΔE [31]. In general, a lower AOS value means more Mn^{3+} in the catalysts, which represents more oxygen vacancies in the catalysts [32]. Meanwhile, the Co 2p$_{3/2}$ spectra are divided into 779.8 and 781.4 eV, which can be corresponded to the Co^{3+} and Co^{2+}, respectively [33]. Similarly, the generation of the oxygen vacancies results in the conversion of some Co^{3+} ions into Co^{2+} [34]. Among the CoMnNiO$_x$ catalysts, CoMnNiO$_x$-S-A exhibits the largest ratios of Mn^{3+}/Mn^{4+} and Co^{2+}/Co^{3+} ratios. Therefore, it demonstrates that the de-aluminum and de-lithium process can induce the generation of the oxygen vacancies in the composite metal oxides. The presence of oxygen vacancy defects can be further confirmed by EPR technology. Due to the complex composition and mixing of the multiple structures, the prepared catalysts are difficult to detect high-quality EPR signals even at low temperature (100 K). Even so, it is observed the CoMnNiO$_x$-S-A catalyst demonstrates a strongly symmetric signal with a g-value of 2.003 (Fig. 3d), which can be attributed to the electrons trapped in the oxygen vacancy defects [35,36].

3.3. Catalytic activity and stability

Figs. 4a and S3a exhibit the light-off curves of propane conversion and CO$_2$ yield over prepared catalysts. It can be seen that CoMnNiO$_x$-S-A
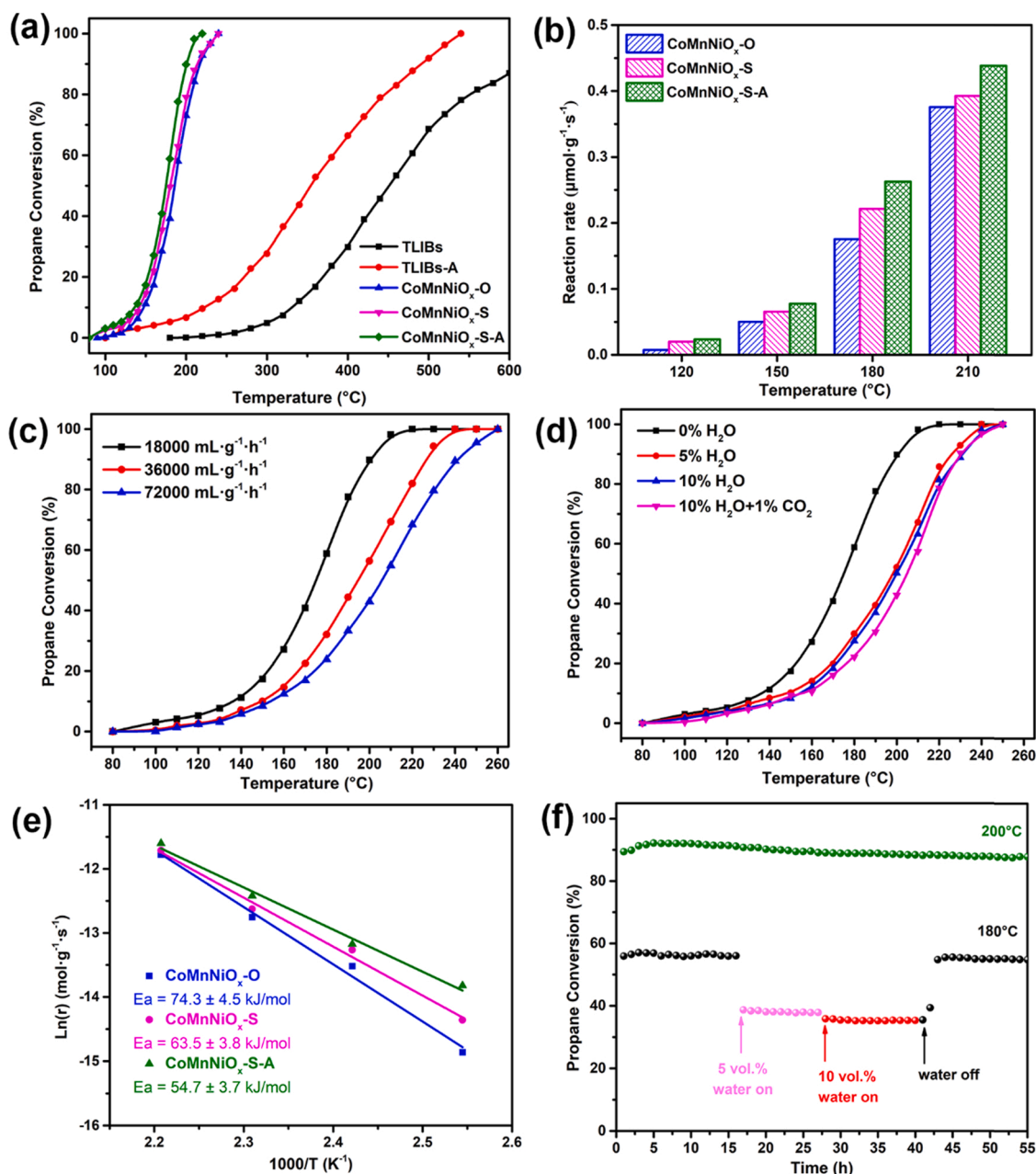
Fig. 4. Catalytic performance and kinetic test of obtained catalysts for propane oxidation. (a) light-off curves, (b) reaction rate, (c) different mass space velocity, (d) different environmental conditions, (e) apparent activation energy (E_a) with 5 vol% H_2O, and (d) stability tests. Conditions: CoMnNiO$_x$-S-A catalyst (c, d, f), 0.2% C_3H_8, 2.5% O_2, balance with N_2, and the WHSV was 18,000 mL g^{-1} h^{-1} (a, b, d, f).

catalyst possesses excellent low-temperature catalytic activity, with the temperatures of 90% propane conversion (T$_{90}$) is 200 °C. Obviously, the alkaline etching process promotes the catalytic activity of propane oxidation, which can be related to the enhanced the number of defects caused by the dissolution of Li$^+$ and Al^{3+}. The reaction rates of three CoMnNiO$_x$ catalysts are calculated, as depicted in Fig. 4b. The comparison order of the reaction rate at 120 °C, 150 °C, 180 °C and 210 °C is CoMnNiO$_x$-S-A > CoMnNiO$_x$-S > CoMnNiO$_x$-O, which indicates that sodium carbonate as the precipitant and alkaline etching present an excellent strategy for preparing the high-performance catalysts for propane oxidation. Compared to our previous study, CoMnNiO$_x$-S-A catalyst exhibits a lower T$_{90}$ value than the highly defective amorphous Co-Mn oxides under the same reaction conditions [22]. According to literature published in recent years (Table S4), CoMnNiO$_x$-S-A catalyst displays excellent catalytic activity in TMOs catalysts in terms of activity

indicators such as T$_{90}$, reaction rate and TOF value, although there is still a gap with the well-performing noble metal catalysts. Considering the complex environmental conditions of practical application, the influences of WHSV, water and CO_2 content are investigated, as shown in Figs. 4c, d and S3. Obviously, the catalytic activity of CoMnNiO$_x$-S-A catalyst is affected by changing the WHSV value and adding high concentration of water and CO_2. It is interesting that the inhibition of activity by water decreases, as the water concentration increases from 5% to 10%. In the meanwhile, the adding CO_2 exhibits a lower inhibitory effect than that of water, demonstrating that the competitive adsorption between CO_2 and reactants is weak.

The apparent activation energies (E_a) of CoMnNiO$_x$ catalysts are calculated from the Arrhenius plots [37]. As shown in Fig. S5a, b, the E_a value increases in the following order: CoMnNiO$_x$-S-A (44.1 kJ/mol) < CoMnNiO$_x$-S (54.2 kJ/mol) < CoMnNiO$_x$-O (69.1 kJ/mol). The
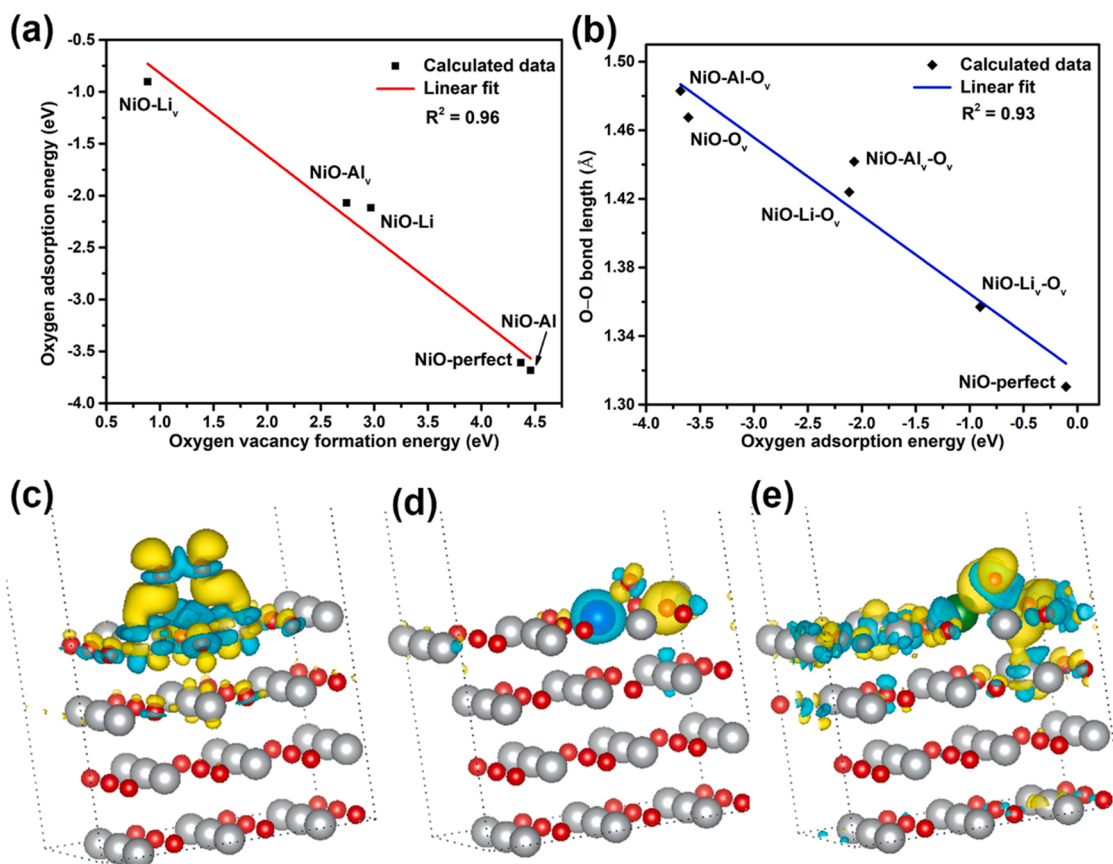
Fig. 5. (a, b) The relationship between formation energy of oxygen vacancy, oxygen adsorption energy and O—O bond length, and the charge density difference of O_2 adsorbed on (c) NiO-perfect, (d) NiO-Al_v-O_v, and (e) NiO-Li_v-O_v. (Gray: Ni atoms; Red: O atoms; Blue: Al atoms; Green: Li atoms; Yellow: electron-rich density; Cyan: electron-deficient density).

lowest E_a value in the CoMnNiO$_x$-S-A catalyst indicates that propane is more easily oxidized by defect-rich CoMnNiO$_x$-S-A catalyst. It can be found that the Ea values are increased while 5 vol% water is added to the reactant gas (Figs. 4e and S5c). Therefore, it can be inferred that the active sites are occupied by water molecules and then the oxidation capacity of propane is reduced.

The stability test of the CoMnNiO$_x$-S-A catalyst is further investigated. As can be observed in Fig. 4f, the propane conversion in the case of CoMnNiO$_x$-S-A catalyst can be maintained around 90% without obvious inactivation for more than 55 h under 200 °C. Water vapor is a common accompanying impurity in the exhaust gas. In the meanwhile, water molecules might compete with the reactants for adsorption, thus, affecting the catalytic activity [38]. In case the concentration of the added water vapor is 1.55 vol% and 3 vol%, the propane conversion is noted to remain almost unchanged at 200 °C (Fig. S3b). In addition, the propane conversion drops from 56% to 38% when 5 vol% water is added, and then descends to 38% when 10 vol% water is added. It is worth mentioning that the activity can be recovered after the water is removed (Fig. 4f). For further investigating the stability of CoMnNiOx-S-A catalyst, the results of three cycle tests shows that that catalytic activity hardly changes (Fig. S6). Based on the above investigations, it reveals that the CoMnNiO$_x$-S-A catalyst possesses an excellent durability, although the catalytic activity is susceptible to partial inhibition under the high-humidity conditions.

3.4. Insights into the role of oxygen vacancy defects by DFT calculations

As discussed above, Al^{3+} and Li^+ are removed from the CoMnNiO$_x$ lattice by the alkaline etching to promote the generation of the oxygen vacancy defects. DFT calculation was adopted to gain theoretical insights into the atomic defect structure and density of the electronic states in CoMnNiO$_x$ catalysts. As NiO is the main crystal form presented in the CoMnNiO$_x$ catalysts, three types of supercell models (NiO, NiO-Al and NiO-Li) were constructed and employed for further investigation. The formation energy of the oxygen vacancy (E_{Ov}) and the oxygen adsorption energy (E_{ads}) represent the general descriptor of activity trends during the catalytic oxidation. The detailed structural models are displayed in Figs. S7 and S8.

Based on the calculation results, the linear relationship analysis between E_{Ov}, E_{ads} and O—O bond length is performed. As illustrated in Fig. 5a, the cation vacancies (Al_v and Li_v) promote the formation of the oxygen vacancies due to a decline in E_{Ov}. However, it can be observed that E_{ads} increases on enhancing E_{Ov}, which indicates a negative correlation between the oxygen vacancy formation capacity and oxygen adsorption intensity. In addition, it is observed that a strong E_{ads} triggers an increase in the O—O bond length in the oxygen vacancies in all models (Fig. 5b), which indicates that a strong E_{ads} contributes to the activation of the oxygen molecules [25]. As reported by Su et al. [39], the high E_{Ov} value inhibits the dissociation of the reactant oxygen, which is consistent with the findings obtained in this study. The comprehensive analysis of both E_{Ov} and E_{ads} reveals that NiO-Al_v and NiO-Li_v possess the best oxygen vacancy forming ability, and NiO-Al_v-O_v and NiO-Li_v-O_v demonstrate a superior oxygen adsorption ability than NiO-perfect.

In order to compare the change in the charge transfer on the CoMnNiO$_x$ catalysts, the charge density differences of the O_2 molecules adsorbed on NiO, NiO-Al_v-O_v (O vacancy near the Al vacancy) and NiO-Li_v-O_v (O vacancy near the Li vacancy) are depicted in Fig. 5c–e. It has been reported that the activation of the oxygen molecules is a critical step in VOCs oxidation [40]. The O_2 molecules adsorbed on NiO-Al_v-O_v
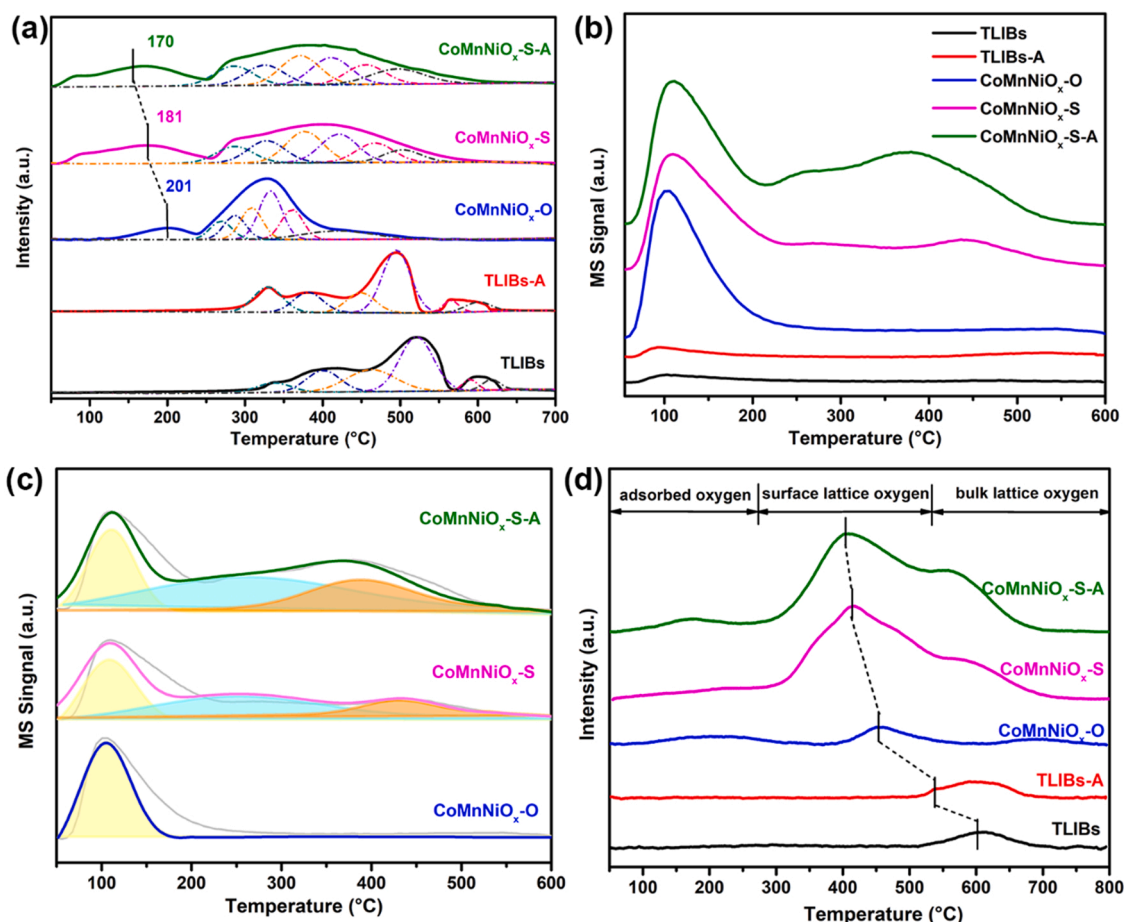
Fig. 6. (a) H_2-TPR, (b, c) NH_3-TPD, and (d) O_2-TPD profiles of prepared catalysts.

and NiO-Li$_v$-O$_v$ exhibit a more obvious electron transfer as compared with NiO-perfect, and the O—O bond lengths in the three models are determined to be 1.44 Å, 1.36 Å and 1.31 Å, respectively. The enlargement of the O—O bond length means a higher degree of oxygen activation, which is conducive for the oxidative activity. In summary, the cation vacancies (Al$_v$ and Li$_v$) generated by the defect enhancement engineering can boost the generation of the surrounding oxygen vacancies, and the oxygen vacancies subsequently facilitate the activation of the oxygen molecules. Therefore, it can be speculated that NiO-Al$_v$-O$_v$ and NiO-Li$_v$-O$_v$ are the main active sites with high activity in the CoMnNiO$_x$-S-A catalyst which modified by the alkaline etching.

3.5. Reducibility and acidity properties

The reducibility of the catalysts is assessed by the H_2-TPR tests. As shown in Fig. 6a, there are three reduction peaks in TLIBs and TLIBs-A catalysts, which can be attributed to the reduction of the chemisorbed oxygen species on oxygen vacancies (150–250 °C) and $M^{3+/4+}$ to $M^{3+/2+}$ and $M^{3+/2+}$ to $M^{2+/0}$ (M=Co, Mn, Ni) (250–350 °C), respectively [41, 42]. Depending on the redox ability of metal cations, the sequence of reduction peaks of metal cation can be divided into $Ni^{3+} \rightarrow Ni^{2+}$, $Mn^{4+} \rightarrow Mn^{3+}$, $Co^{3+} \rightarrow Co^{2+}$, $Ni^{2+} \rightarrow Ni^0$, $Co^{2+} \rightarrow Co^0$ and $Mn^{3+} \rightarrow Mn^{2+}$ [43]. It is interesting that the reduction temperatures of both chemically adsorbent oxygen and metal cations move to low temperature. As shown in Table S2, an ascending order of the reduction peaks of the chemisorbed oxygen species in three CoMnNiO$_x$ catalysts can be written as: CoMnNiO$_x$-S-A (170 °C) < CoMnNiO$_x$-S (181 °C) < CoMnNiO$_x$-O (201 °C). Furthermore, the amount of total hydrogen consumption and catalytic activity for all catalysts displayed an incremental trend in the same order. Among them, the total hydrogen consumption of

CoMnNiO$_x$-S-A (2.65 mmol g$^{-1}_{cat}$) is larger than that of CoMnNiO$_x$-S (2.35 mmol g$^{-1}_{cat}$), CoMnNiO$_x$-O (1.81 mmol g$^{-1}_{cat}$), TLIBs-A (1.79 mmol g$^{-1}_{cat}$) and TLIBs (1.62 mmol g$^{-1}_{cat}$). This means that the enhancement of oxygen vacancies improves the number of reducible metal cation sites. Overall, the oxygen vacancy enhancement efficiently promotes the reducibility of the developed catalysts.

The intensity and quantity of the acid sites on the surface of the catalyst are also the vital determinants for VOCs oxidation. Fig. 6b, c and Table S3 demonstrate the findings from the NH_3-TPD analysis, and the three desorption peaks can be attributed to the physisorbed NH_3 (ca. 100 °C), weak acidic sites (ca. 250 °C) and strong acidic sites (ca. 400 °C), respectively [44]. As observed, CoMnNiO$_x$-S-A possesses a higher extent of acid sites than CoMnNiO$_x$-O and CoMnNiO$_x$-S, especially the strong acid sites. This significantly indicates that acid sites are enhanced by the de-aluminum and de-lithium process. As is well known, the rate-controlling step during the propane oxidation reaction is the first C—H bond activation [9,45]. In general, acid sites are beneficial to the dissociation and activation of the robust C—H bonds. For example, Yue et al. have reported that the Lewis acid sites are able to activate the C—H bond of propane [46]. Consequently, combined with the structure and activity data of the catalysts, it can be proposed that the low-temperature reducibility and acid sites can accelerate the activation of propane.

3.6. Oxygen mobility analysis

During the propane oxidation reaction, the mobility of the reactive oxygen species serves an intuitive correlation with the catalytic activity. Therefore, the oxygen mobility of the catalysts is analyzed by performing the O_2-TPD tests (Fig. 6d). The desorbed oxygen species can be
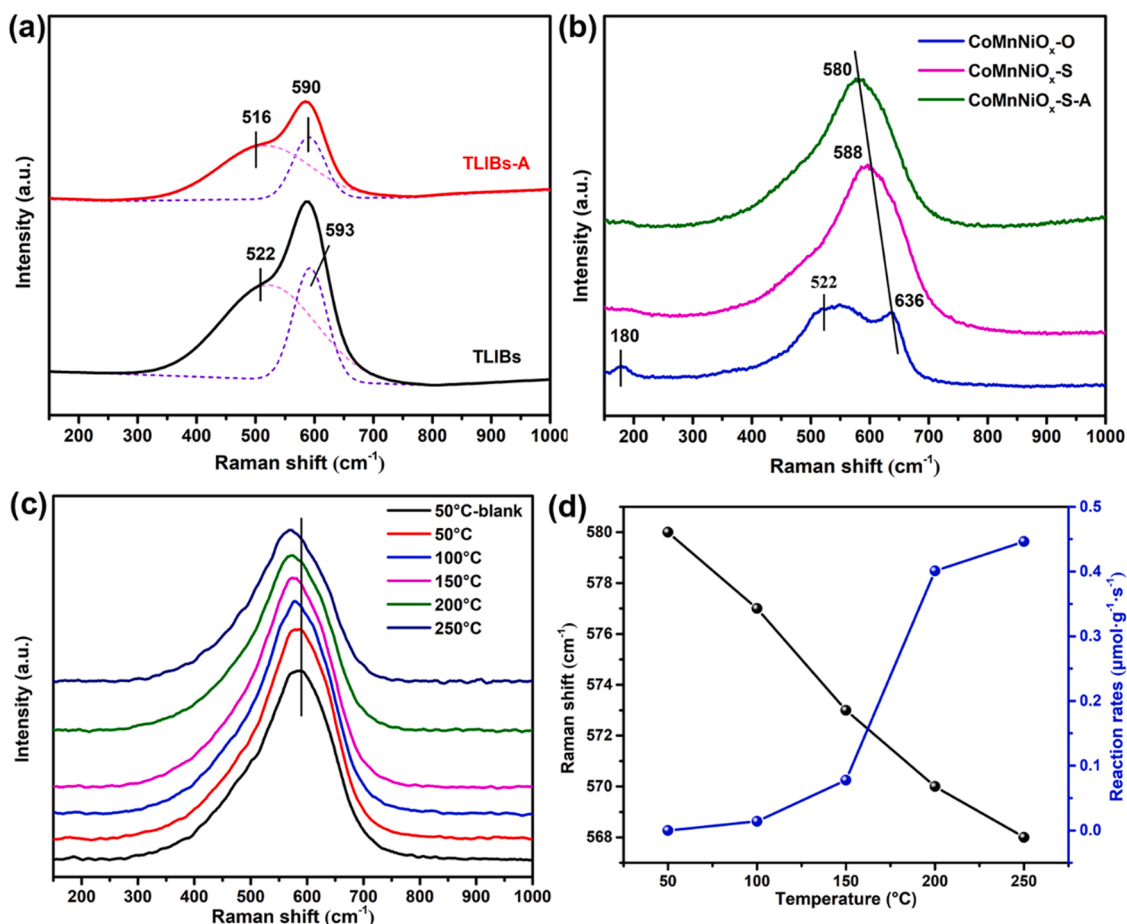
Fig. 7. (a, b) *Ex situ* Raman spectra of prepared catalysts, (c) in situ Raman spectra and (d) the change of Raman shift over CoMnNiO$_x$-S-A catalyst at different temperatures.

classified as the chemisorbed oxygen adsorbed on the oxygen vacancies (100–300 °C), surface lattice oxygen (300–600 °C) and bulk lattice oxygen (>600 °C) [47]. The CoMnNiO$_x$-S-A catalyst exhibits the highest content of both chemisorbed oxygen and surface lattice oxygen. Moreover, the release temperatures of the surface lattice oxygen are arranged in the following descending order: CoMnNiO$_x$-O > CoMnNiO$_x$-S > CoMnNiOx-S-A, which is consistent with the order of the catalytic activity. Therefore, it can be concluded that the surface lattice oxygen is the main reactive oxygen species during the propane oxidation reaction, and it follows the Mars-van-Krevelen (MvK) mechanism as reported in most literature [22,33,45,48]. Apparently, the presence of the oxygen vacancies promotes the reducibility and oxygen mobility of the developed catalysts, thereby enhancing the catalytic activity.

The Raman spectroscopy is a powerful tool to characterize the vibration modes of the metal oxygen (M—O) bond in the TMOs. The structural differences in the prepared catalysts are probed, as displayed in Fig. 7a, b. The Raman bands located at 522 cm^{-1} and 593 cm^{-1} in TLIBs and TLIBs-A are assigned to the δ(O-M-O) vibrations and ν(MO$_6$) vibrations, respectively [49]. In the CoMnNiO$_x$ catalysts, the main Raman band at 580 cm^{-1} can be attributed to the first-order transverse optical phonon modes of NiO [25]. Specifically, a new peak at 180 cm^{-1} is observed in the CoMnNiO$_x$-O catalyst, which represents the typical Co (II)-O vibration in the tetrahedral coordination structure [50]. The observed phenomenon can be attributed to the enrichment of the cobalt elements by the oxalic acid precipitation. The red-shift of the Raman band exists in the catalysts after the alkaline etching, which signifies that the enhancement of the oxygen vacancy defects in the CoMnNiO$_x$ catalysts can weaken the M—O bond.

For revealing the relationship between the M—O bond and catalytic

activity, in situ Raman technology is used to detect the structural changes in the CoMnNiO$_x$-S-A catalyst under the real reaction conditions. As shown in Fig. 7c, the main peak gradually red-shifts as the reaction temperature is increased. The quantitative comparison in Fig. 7d depicts a negative correlation between the Raman shift and reaction rate of propane oxidation. Overall, the obtained results demonstrate that the weakening of the M—O bonds during the reaction is beneficial for the mobility and reactivity of the surface lattice oxygen, which significantly affect the efficiency of propane oxidation [41].

3.7. Degradation pathway of propane

In situ DRIFTS results of propane oxidation on prepared catalysts at 200 °C are collected as shown in Fig. 8. The absorption peaks at 2967 cm^{-1}, 2900 cm^{-1} and 2873 cm^{-1} are the typical C-H vibration of -CH$_3$ in gaseous propane and -CH$_2$/-CH$_3$ in dissociate adsorbed propane [22]. According to the range of 1000–1800 cm^{-1}, the presence of oxygenated or unsaturated intermediate species in propane oxidation can be identified. Obviously, there are few intermediate species peaks on the TLIBs and TLIBs catalysts due to its weak ability to activate propane and deep oxidation. On CoMnNiO$_x$ catalysts, the peaks at 1640 cm^{-1} and 1468 cm^{-1} are assigned to the C=C stretching and C-H bending mode of propene [51]. The peak shifts at 1640 cm^{-1} of the CoMnNiO$_x$-S and CoMnNiO$_x$-S-A catalysts indicate the adsorption strength of propene is different. It is interesting that there are only two peaks of carboxylate species (1554 cm^{-1} and 1352 cm^{-1}) on CoMnNiO$_x$-S-A catalyst [52], which can be attributed to the abundant oxygen vacancy defects promoting the dissociation and deep oxidation of robust C—H bonds. And finally, the peaks at 1230–1300 cm^{-1} can be classified as the bidentate
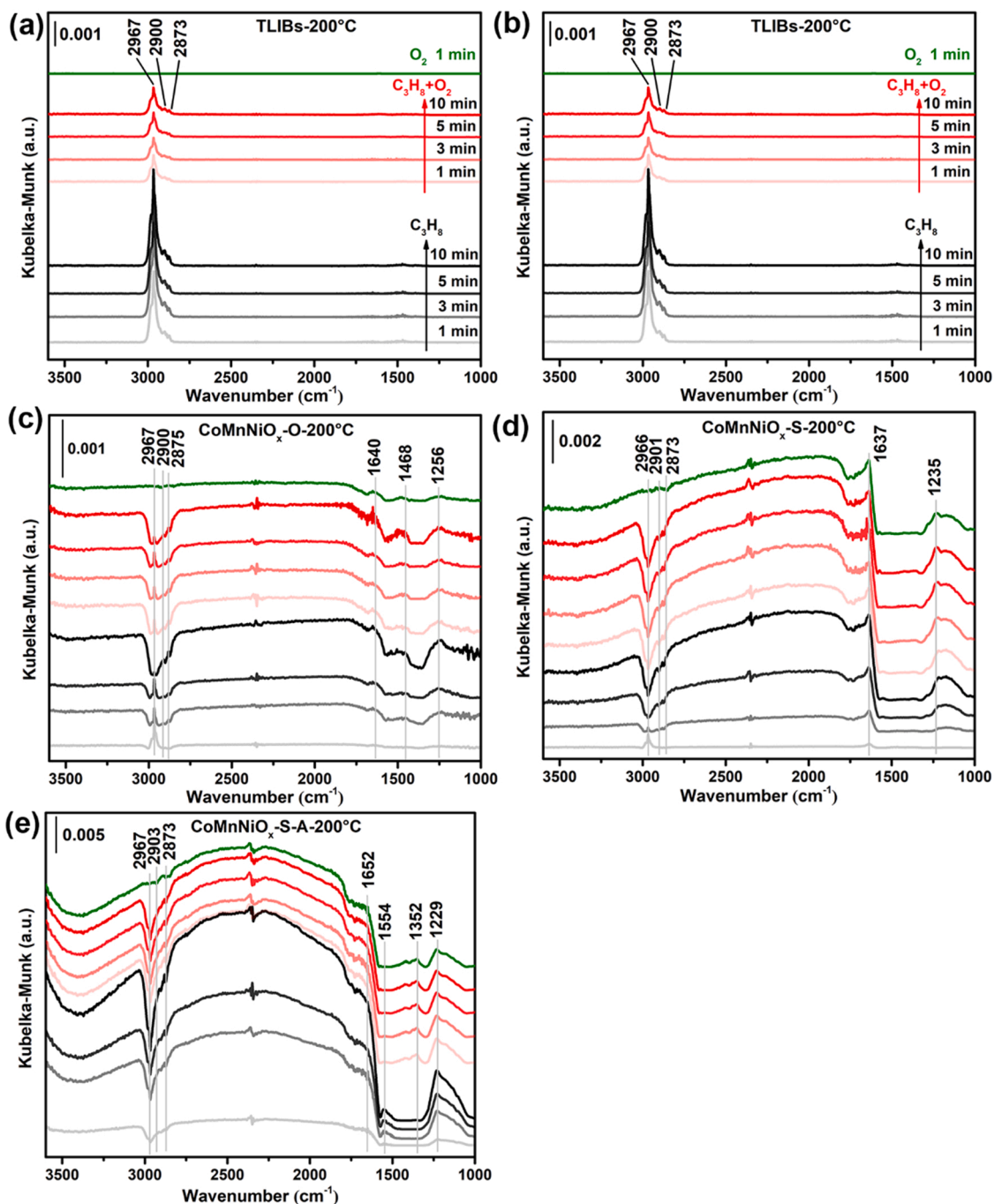
Fig. 8. *In situ* DRIFTS of propane oxidation over (a) TLIBs, (b) TLIBs-A, (c) CoMnNiO$_x$-O, (d) CoMnNiO$_x$-S and (e) CoMnNiO$_x$-S-A catalysts at 200 °C (0.2% propane, 2.5% O$_2$ and balance N$_2$).

carbonate and there are significant adsorption peaks of CO$_2$ at 2300–2400 cm^{-1} [52]. To sum up, the degradation of propane oxidation over CoMnNiO$_x$ catalysts goes through the processes of propene to carboxylate, carbonate species and finally to CO$_2$ and H$_2$O (Scheme 1).

4. Discussion

In this study, the alkaline etching of prepared catalysts derived from waste TLIBs is proved to not only enhancing the oxygen vacancy defects of CoMnNiO$_x$ catalysts but also boosting their catalytic performance in propane oxidation. The result of XRD shows that the derived CoMnNiO$_x$ catalysts mainly presents the NiO crystal structure with low crystallization. It is necessary to remove Al and Li impurities from waste LIBs in

order to further improve catalytic activity. The result of ICP-OES proves that the Al^{3+} and Li$^+$ can be selectively dissolved in NaOH solutions. According to the above results, it can be obtained that Al^{3+} and Li$^+$ can be adopted as atom templates to generate the metal cationic vacancies during the de-aluminum and de-lithium process, which will further induce the generation of oxygen vacancies. And then, the hypothesis about oxygen vacancy enhancement is supported by XPS, EPR and DFT calculations.

According to the result of catalytic performance for propane oxidation, CoMnNiO$_x$-S-A catalyst exhibits superior activity than other prepared catalysts, with T$_{90}$ of 200 °C at a WHSV of 18,000 mL g^{-1} h^{-1}. It is interesting that catalytic activities after alkaline etching are improved in both TLIBs and CoMnNiO$_x$-S catalysts. H$_2$-TPR and O$_2$-TPD results show
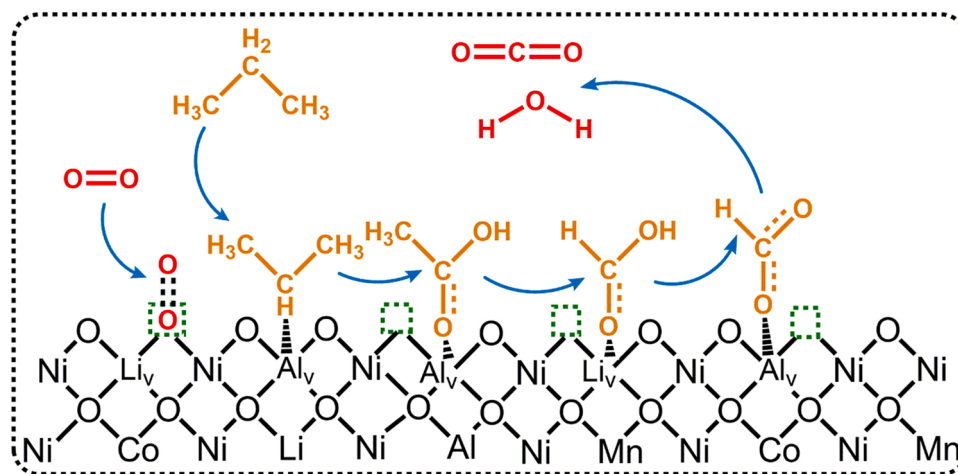
Scheme 1. Proposed mechanism for propane oxidation over defect enhanced CoMnNiO$_x$ catalyst.

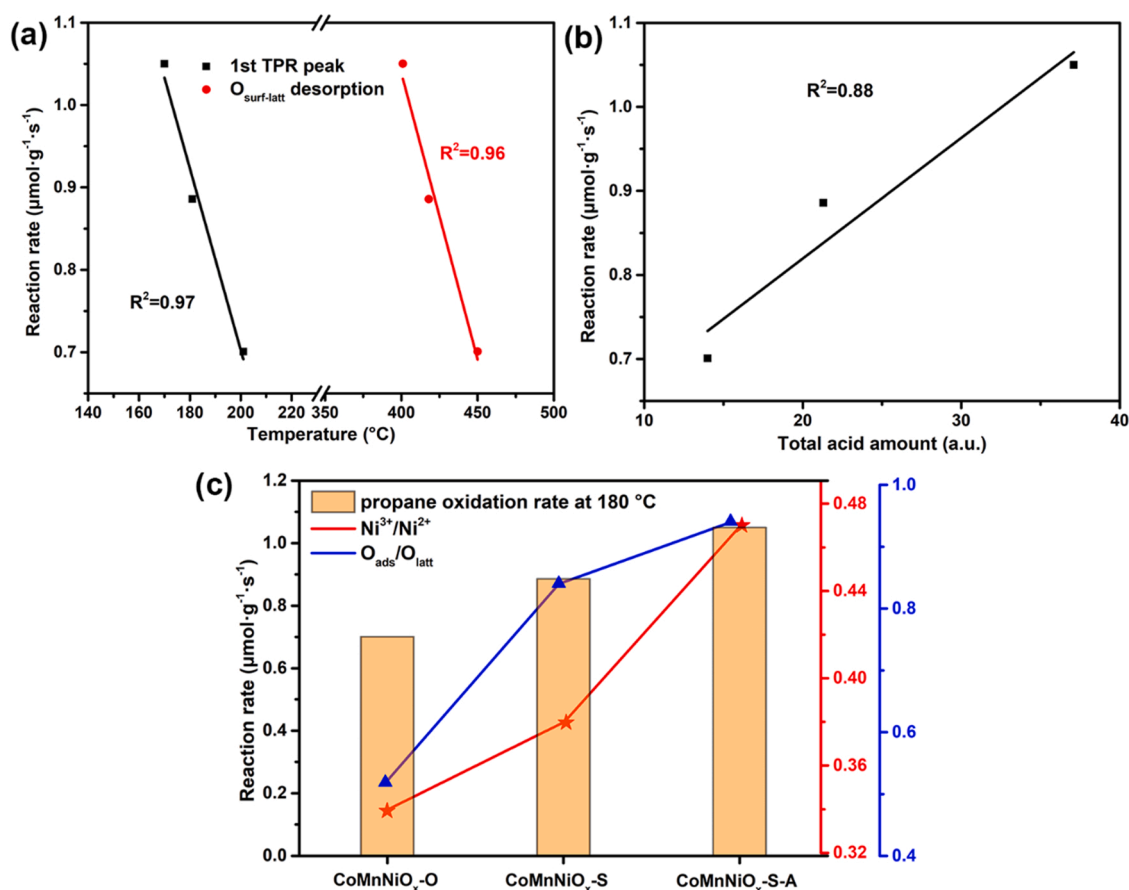**Fig. 9.** The relationship between the propane oxidation rate at 180 °C and (a) the low temperature reducibility and desorption temperature of surface lattice oxygen, (b) the total acid amount, and (c) the oxygen vacancy defects of CoMnNiO$_x$ catalysts.

that both the reduction of chemisorption oxygen and the desorption of surface lattice oxygen move toward low temperature with the increase of oxygen vacancies. Fig. 9a indicates both the reduction of chemisorption oxygen and the desorption of surface lattice oxygen have a strong linear relationship with catalytic reaction rates of propane oxidation. Furthermore, the number of acid sites is positively correlated with the catalytic activity (Fig. 9b), demonstrating that acid sites play a significant role in the activation of C—H bond which is the rate-determining step of propane oxidation [9,45].

As demonstrated in our previous study [22], oxygen vacancies can

effectively regulate the reducibility and lattice oxygen mobility of TMOs catalysts. Moreover, at the atomic level, the acid sites on the metal oxides are the terminal unsaturated metal cations formed by the rupture of the metal oxygen bond on the exposed surface. In other words, the formation of oxygen vacancies will enhance the acidity of TMOs catalysts. As shown in Fig. 9c, the main indicators of oxygen vacancy (Ni^{3+}/Ni^{2+} and O$_{ads}$/O$_{latt}$) exhibit a close correlation with catalytic activity, which confirms that the defect enhancement engineering of oxygen vacancy exists a crucial boosting effect on propane oxidation.

5. Conclusions

In this work, the CoMnNiO$_x$ catalysts were prepared from waste TLIBs and exhibited excellent catalytic activity in propane oxidation reactions. Defect enhancement engineering resulting from alkaline etching further promoted the catalytic activity, and the T$_{90}$ of propane oxidation in CoMnNiO$_x$-S-A catalyst was only 200 °C at a WHSV of 18,000 mL g^{-1} h^{-1}. Meaningfully, the de-aluminum and de-lithium process by alkaline etching was the main reason for the increase of oxygen vacancy defects. The results of DFT calculation revealed that the oxygen vacancies near the aluminum and lithium vacancies (NiO-Al$_v$-O$_v$ and NiO-Li$_v$-O$_v$) were more likely to promote the dissociation and activation of the oxygen molecules. Furthermore, the presence of the abundant oxygen vacancies enhanced the reducibility, acidity and lattice oxygen mobility of the CoMnNiO$_x$-S-A catalyst, which are the critical factors in the boosting propane oxidation. Finally, propane oxidation followed the MvK mechanism and the degradation path goes through the processes of propene to carboxylate, carbonate species and finally to CO$_2$ and H$_2$O.

CRediT authorship contribution statement

Ganggang Li: Investigation, Methodology, Formal analysis, Data curation, Validation, Writing – original draft. **Kai He:** Data curation, Writing – review & editing. **Fenglian Zhang:** Formal analysis, Writing – review & editing. **Guoxia Jiang:** Formal analysis, Writing – review & editing. **Zeyu Zhao:** Data curation. **Zhongshen Zhang:** Supervision, Writing – review & editing, Funding acquisition. **Jie Cheng:** Conceptualization, Formal analysis, Funding acquisition. **Zhengping Hao:** Conceptualization, Investigation, Supervision, Writing – review & editing, Funding acquisition.

Declaration of Competing Interest

The authors declare that they have no known competing financial interests or personal relationships that could have appeared to influence the work reported in this paper.

Acknowledgments

Appendix A. Supplementary material

Supplementary data associated with this article can be found in the online version at doi:10.1016/j.apcatb.2022.121231.

References

[1] I. Morse, A dead battery dilemma, Science 372 (2021) 780–783.
[2] G. Harper, R. Sommerville, E. Kendrick, L. Driscoll, P. Slater, R. Stolkin, A. Walton, P. Christensen, O. Heidrich, S. Lambert, A. Abbott, K. Ryder, L. Gaines, P. Anderson, Recycling lithium-ion batteries from electric vehicles, Nature 575 (2019) 75–86.
[3] J. Dunn, M. Slattery, A. Kendall, H. Ambrose, S. Shen, Circularity of lithium-ion battery materials in electric vehicles, Environ. Sci. Technol. 55 (2021) 5189–5198.
[4] H. Wang, R. Hao, L. Fang, L. Nie, Z. Zhang, Z. Hao, Study on emissions of volatile organic compounds from a typical coking chemical plant in China, Sci. Total Environ. 752 (2021), 141927.
[5] M. Guo, K. Li, L. Liu, H. Zhang, W. Guo, X. Hu, X. Meng, J. Jia, T. Sun, Manganese-based multi-oxide derived from spent ternary lithium-ions batteries as high-efficient catalyst for VOCs oxidation, J. Hazard. Mater. 380 (2019), 120905.
[6] M. Guo, K. Li, L. Liu, H. Zhang, W. Guo, X. Hu, X. Min, J. Jia, T. Sun, Insight into a sustainable application of spent lithium-ion cobaltate batteries: preparation of a cobalt-based oxide catalyst and its catalytic performance in toluene oxidation, Ind. Eng. Chem. Res. 59 (2020) 194–204.
[7] M. Guo, K. Li, H. Zhang, X. Min, J. Liang, X. Hu, W. Guo, J. Jia, T. Sun, Promotional removal of oxygenated VOC over manganese-based multi oxides from spent lithium-ions manganate batteries: Modification with Fe, Bi and Ce dopants, Sci. Total Environ. 740 (2020), 139951.
[8] X. Min, M. Guo, L. Liu, L. Li, J.-n Gu, J. Liang, C. Chen, K. Li, J. Jia, T. Sun, Synthesis of MnO$_2$ derived from spent lithium-ion batteries via advanced oxidation and its application in VOCs oxidation, J. Hazard. Mater. 406 (2021), 124743.
[9] Y. Liu, X. Li, W. Liao, A. Jia, Y. Wang, M. Luo, J. Lu, Highly active Pt/BN catalysts for propane combustion: the roles of support and reactant-induced evolution of active sites, ACS Catal. 9 (2019) 1472–1481.
[10] W.-M. Liao, X.-X. Fang, B.-H. Cen, J. Chen, Y.-R. Liu, M.-F. Luo, J.-Q. Lu, Deep oxidation of propane over WO$_3$ - promoted Pt/BN catalysts: the critical role of Pt - WO$_3$ interface, Appl. Catal. B 272 (2020), 118858.
[11] Y. Jian, M. Tian, C. He, J. Xiong, Z. Jiang, H. Jin, L. Zheng, R. Albilali, J.-W. Shi, Efficient propane low-temperature destruction by Co$_3$O$_4$ crystal facets engineering: unveiling the decisive role of lattice and oxygen defects and surface acid-base pairs, Appl. Catal. B 283 (2021), 119657.
[12] Y. Wang, S. Aghamohammadi, D. Li, K. Li, R. Farrauto, Structure dependence of Nb$_2$O$_{5-x}$ supported manganese oxide for catalytic oxidation of propane: Enhanced oxidation activity for MnO$_x$ on a low surface area Nb$_2$O$_{5-x}$, Appl. Catal. B 244 (2019) 438–447.
[13] X. Zhang, R. You, D. Li, T. Cao, W. Huang, Reaction sensitivity of ceria morphology effect on Ni/CeO$_2$ catalysis in propane oxidation reactions, ACS Appl. Mater. Interfaces 9 (2017) 35897–35907.
[14] Z. Hu, S. Qiu, Y. You, Y. Guo, L. Wang, W. Zhan, G. Lu, Hydrothermal synthesis of NiCeO$_x$ nanosheets and its application to the total oxidation of propane, Appl. Catal. B 225 (2018) 110–120.
[15] J. Bae, D. Shin, H. Jeong, C. Choe, Y. Choi, J.W. Han, H. Lee, Facet-dependent Mn doping on shaped Co$_3$O$_4$ crystals for catalytic oxidation, ACS Catal. 11 (2021) 11066–11074.
[16] C. Xie, D. Yan, H. Li, S. Du, W. Chen, Y. Wang, Y. Zou, R. Chen, S. Wang, Defect chemistry in heterogeneous catalysis: recognition, understanding, and utilization, ACS Catal. 10 (2020) 11082–11098.
[17] N. Zhang, X. Li, H. Ye, S. Chen, H. Ju, D. Liu, Y. Lin, W. Ye, C. Wang, Q. Xu, J. Zhu, L. Song, J. Jiang, Y. Xiong, Oxide defect engineering enables to couple solar energy into oxygen activation, J. Am. Chem. Soc. 138 (2016) 8928–8935.
[18] M. Wu, S. Chen, W. Xiang, Oxygen vacancy induced performance enhancement of toluene catalytic oxidation using LaFeO$_3$ perovskite oxides, Chem. Eng. J. 387 (2020), 124101.
[19] Y. Zhang, L. Tao, C. Xie, D. Wang, Y. Zou, R. Chen, Y. Wang, C. Jia, S. Wang, Defect engineering on electrode materials for rechargeable batteries, Adv. Mater. 32 (2020), 1905923.
[20] W. Si, Y. Wang, Y. Peng, J. Li, Selective dissolution of A-site cations in ABO$_3$ perovskites: a new path to high-performance catalysts, Angew. Chem. Int. Ed. 54 (2015) 7954–7957.
[21] K. He, Z.-Y. Zhang, L. Alai, F.-S. Zhang, A green process for exfoliating electrode materials and simultaneously extracting electrolyte from spent lithium-ion batteries, J. Hazard. Mater. 375 (2019) 43–51.
[22] G. Li, N. Li, Y. Sun, Y. Qu, Z. Jiang, Z. Zhao, Z. Zhang, J. Cheng, Z. Hao, Efficient defect engineering in Co-Mn binary oxides for low-temperature propane oxidation, Appl. Catal. B 282 (2021), 119512.
[23] J. Kuljiraseth, A. Wangriya, J.M.C. Malones, W. Klysubun, S. Jitkarnka, Synthesis and characterization of AMO LDH-derived mixed oxides with various Mg/Al ratios as acid–base catalysts for esterification of benzoic acid with 2-ethylhexanol, Appl. Catal. B 243 (2019) 415–427.
[24] J. You, W. Sun, S. Su, Z. Ao, C. Liu, G. Yao, B. Lai, Degradation of bisphenol A by peroxymonosulfate activated with oxygen vacancy modified nano-NiO-ZnO composite oxides: a typical surface-bound radical system, Chem. Eng. J. 400 (2020), 125915.
[25] X. Xu, L. Li, J. Huang, H. Jin, X. Fang, W. Liu, N. Zhang, H. Wang, X. Wang, Engineering Ni^{3+} cations in NiO lattice at the atomic level by Li$^+$ doping: the roles of Ni^{3+} and oxygen species for CO oxidation, ACS Catal. 8 (2018) 8033–8045.
[26] R. Zheng, C. Shu, J. Li, A. Hu, N. Chen, M. Li, J. Long, Oxygen vacancy engineering of vertically aligned NiO nanosheets for effective CO$_2$ reduction and capture in Li-CO$_2$ battery, Electrochim. Acta 383 (2021), 138359.
[27] H. Liu, Y. Yang, J. Zhang, Reaction mechanism and kinetics of lithium ion battery cathode material LiNiO$_2$ with CO$_2$, J. Power Sources 173 (2007) 556–561.
[28] H. Deng, S. Kang, J. Ma, L. Wang, C. Zhang, H. He, Role of structural defects in MnO$_x$ promoted by Ag doping in the catalytic combustion of volatile organic compounds and ambient decomposition of O$_3$, Environ. Sci. Technol. 53 (2019) 10871–10879.
[29] Y. Zheng, R. Zhang, P. Vanaphuti, J. Fu, Z. Yang, Y. Wang, Unveiling the influence of carbon impurity on recovered NCM622 cathode material, ACS Sustain. Chem. Eng. 9 (2021) 6087–6096.
[30] Y. Sun, X. Zhang, N. Li, X. Xing, H. Yang, F. Zhang, J. Cheng, Z. Zhang, Z. Hao, Surface properties enhanced Mn$_x$AlO oxide catalysts derived from Mn$_x$Al layered double hydroxides for acetone catalytic oxidation at low temperature, Appl. Catal. B 251 (2019) 295–304.
[31] C. He, Y. Wang, Z. Li, Y. Huang, Y. Liao, D. Xia, S. Lee, Facet engineered α-MnO$_2$ for efficient catalytic ozonation of odor CH$_3$SH: oxygen vacancy-induced active centers and catalytic mechanism, Environ. Sci. Technol. 54 (2020) 12771–12783.
[32] J. Liu, Y. Wei, P.-Z. Li, P. Zhang, W. Su, Y. Sun, R. Zou, Y. Zhao, Experimental and theoretical investigation of mesoporous MnO$_2$ nanosheets with oxygen vacancies for high-efficiency catalytic DeNO$_x$, ACS Catal. 8 (2018) 3865–3874.

[33] Z. Zhu, G. Lu, Z. Zhang, Y. Guo, Y. Guo, Y. Wang, Highly active and stable Co₃O₄/ZSM-5 catalyst for propane oxidation: effect of the preparation method, ACS Catal. 3 (2013) 1154–1164.

[34] L. Xu, Q. Jiang, Z. Xiao, X. Li, J. Huo, S. Wang, L. Dai, Plasma-engraved Co₃O₄ nanosheets with oxygen vacancies and high surface area for the oxygen evolution reaction, Angew. Chem. Int. Ed. 55 (2016) 5277–5281.

[35] L. Liu, Q. Liu, Y. Wang, J. Huang, W. Wang, L. Duan, X. Yang, X. Yu, X. Han, N. Liu, Nonradical activation of peroxydisulfate promoted by oxygen vacancy-laden NiO for catalytic phenol oxidative polymerization, Appl. Catal. B 254 (2019) 166–173.

[36] T. Gan, J. Yang, D. Morris, X. Chu, P. Zhang, W. Zhang, Y. Zou, W. Yan, S.-H. Wei, G. Liu, Electron donation of non-oxide supports boosts O₂ activation on nano-platinum catalysts, Nat. Commun. 12 (2021) 2741.

[37] X. Weng, P. Sun, Y. Long, Q. Meng, Z. Wu, Catalytic oxidation of chlorobenzene over MnₓCe₁₋ₓO₂/HZSM-5 catalysts: a study with practical implications, Environ. Sci. Technol. 51 (2017) 8057–8066.

[38] F. Bi, X. Zhang, J. Chen, Y. Yang, Y. Wang, Excellent catalytic activity and water resistance of UiO-66-supported highly dispersed Pd nanoparticles for toluene catalytic oxidation, Appl. Catal. B 269 (2020), 118767.

[39] H.-Y. Su, X. Ma, K. Sun, C. Sun, Y. Xu, F. Calle-Vallejo, Trends in C-O and N-O bond scission on rutile oxides described by oxygen vacancy formation energies, Chem. Sci. 11 (2020) 4119–4124.

[40] S. Zhao, Y. Wen, X. Liu, X. Pen, F. Lü, F. Gao, X. Xie, C. Du, H. Yi, D. Kang, X. Tang, Formation of active oxygen species on single-atom Pt catalyst and promoted catalytic oxidation of toluene, Nano Res. 13 (2020) 1544–1551.

[41] Y. Shen, J. Deng, S. Impeng, S. Li, T. Yan, J. Zhang, L. Shi, D. Zhang, Boosting toluene combustion by engineering Co–O strength in cobalt oxide catalysts, Environ. Sci. Technol. 54 (2020) 10342–10350.

[42] Q. Meng, W. Wang, X. Weng, Y. Liu, H. Wang, Z. Wu, Active oxygen species in Laₙ₊₁NiₙO₃ₙ₊₁ layered perovskites for catalytic oxidation of toluene and methane, J. Phys. Chem. C 120 (2016) 3259–3266.

[43] H. Ziaei-Azad, A. Khodadadi, P. Esmaeilnejad-Ahranjani, Y. Mortazavi, Effects of Pd on enhancement of oxidation activity of LaBO₃ (B=Mn, Fe, Co and Ni)

pervoskite catalysts for pollution abatement from natural gas fueled vehicles, Appl. Catal. B 102 (2011) 62–70.

[44] S.A. Skarlis, D. Berthout, A. Nicolle, C. Dujardin, P. Granger, Multisite modeling of NH₃ adsorption and desorption over Fe-ZSM5, J. Phys. Chem. C 116 (2012) 8437–8448.

[45] T. Zhang, X. Lang, A. Dong, X. Wan, S. Gao, L. Wang, L. Wang, W. Wang, Difference of oxidation mechanism between light C3-C4 alkane and alkene over mullite YMn₂O₅ oxides catalyst, ACS Catal. 10 (2020) 7269–7282.

[46] Y. Yue, J. Fu, C. Wang, P. Yuan, X. Bao, Z. Xie, J.-M. Basset, H. Zhu, Propane dehydrogenation catalyzed by single Lewis acid site in Sn-Beta zeolite, J. Catal. 395 (2021) 155–167.

[47] X. Dai, X. Wang, Y. Long, S. Pattisson, Y. Lu, D.J. Morgan, S.H. Taylor, J.H. Carter, G.J. Hutchings, Z. Wu, X. Weng, Efficient elimination of chlorinated organics on a phosphoric acid modified CeO₂ catalyst: a hydrolytic destruction route, Environ. Sci. Technol. 53 (2019) 12697–12705.

[48] G. Chai, W. Zhang, L.F. Liotta, M. Li, Y. Guo, A. Giroir-Fendler, Total oxidation of propane over Co₃O₄-based catalysts: elucidating the influence of Zr dopant, Appl. Catal. B 298 (2021), 120606.

[49] P. Lanz, C. Villevieille, P. Novák, Ex situ and in situ Raman microscopic investigation of the differences between stoichiometric LiMO₂ and high-energy xLi₂MnO₃·(1–x)LiMO₂ (M = Ni, Co, Mn), Electrochim. Acta 130 (2014) 206–212.

[50] L. Ma, S. Chen, H. Li, Z. Ruan, Z. Tang, Z. Liu, Z. Wang, Y. Huang, Z. Pei, J. A. Zapien, C. Zhi, Initiating a mild aqueous electrolyte Co₃O₄/Zn battery with 2.2 V-high voltage and 5000-cycle lifespan by a Co(iii) rich-electrode, Energy Environ. Sci. 11 (2018) 2521–2530.

[51] G. Liu, Z.-J. Zhao, T. Wu, L. Zeng, J. Gong, Nature of the active sites of VOₓ/Al₂O₃ catalysts for propane dehydrogenation, ACS Catal. 6 (2016) 5207–5214.

[52] Z. Hu, X. Liu, D. Meng, Y. Guo, Y. Guo, G. Lu, Effect of ceria crystal plane on the physicochemical and catalytic properties of Pd/ceria for CO and propane oxidation, ACS Catal. 6 (2016) 2265–2279.